Effect of incoming flow conditions on air lubrication regimes

Nikolaidou, Lina; Laskari, Angeliki; van Terwisga, Tom; Poelma, Christian

DOI
10.1016/j.ijmultiphaseflow.2024.104948

Publication date
2024

Document Version
Final published version

Published in
International Journal of Multiphase Flow

International Journal of Multiphase Flow 180 (2024) 104948

Contents lists available at ScienceDirect

International Journal of Multiphase Flow

journal homepage: www.elsevier.com/locate/ijmulflow

Effect of incoming flow conditions on air lubrication regimes

Lina Nikolaidou [a,*], Angeliki Laskari [a], Tom van Terwisga [b,c], Christian Poelma [a]

[a] Process & Energy (Faculty Mechanical Engineering, Delft University of Technology), Mekelweg 2, Delft, 2628CD, The Netherlands
[b] Maritime and Transport Technology (Faculty Mechanical Engineering, Delft University of Technology), Mekelweg 2, Delft, 2628CD, The Netherlands
[c] Maritime Research Institute of the Netherlands (MARIN), Haagsteeg 2, Wageningen, 6708PM, The Netherlands

ARTICLE INFO

Keywords:
Air layer
Air cavity
Turbulent boundary layer
Regime transition

ABSTRACT

Different air phase regimes are formed by controlled air injection in a spatially developing flat plate turbulent boundary layer (TBL). The air is introduced via a slot type injector without the use of a backward-facing step or cavitator upstream of the air injection position. The effect of different incoming liquid flow characteristics on the different regimes is investigated by varying both the liquid freestream velocity and the incoming TBL thickness. The latter is realized through changing the position of the air injection along the length of the water tunnel facility. That resulted in a downstream distance based Reynolds number from 1 to 5 million. Three different air phase regimes are identified under different air flow rates and freestream velocities: the bubbly regime, the transitional, and the air layer regime. The morphological differences of each one are described and quantitative analysis is performed based on the non-wetted area in each condition. The incoming TBL as well as the flow around the air layer are measured with planar particle image velocimetry. The latter enabled the determination of the air layer thickness. In addition, the ratio of the air layer to the incoming boundary layer thickness t_{air}/δ is also calculated ($\approx 0.04 - 0.5$). This is a significant dimensionless parameter for scaling, which indicates the extent to which the air layer is embedded within the incoming TBL. Depending on the incoming flow conditions, a two or three branch air layer is formed. The length of the air layer is found to increase with increasing liquid freestream velocities. A good agreement between the air layer length and a half gravity wave predicted by the dispersion relation is found. An increase of the air layer length is observed with a decreasing incoming TBL thickness. This is attributed to a decrease in the local mean velocity at the air–water interface due to the TBL growth. Finally, increasing the incoming TBL thickness delays the onset of the air layer regime.

1. Introduction

In light of the emissions reduction goals set by the International Maritime Organization (IMO, 2023), the shipping industry is under increased pressure to implement sustainable solutions. Minimizing the friction or viscous resistance beneath the ship's hull can play a crucial role in reaching this objective. Friction drag accounts on average for 70% of the overall resistance of a surface ship (Larsson, 2010), with the potential to reach 85% for low-speed displacement vessels (Woud and Stapersma, 2002). Therefore, reducing this drag could lead to fuel cost savings and a lower environmental impact.

Multiple passive and active drag reduction methods have been investigated over the past years. Passive methods do not require the addition of mass, momentum or energy to reduce the drag. These include the application of super-hydrophobic coatings and ribblets/textured surfaces (Xu et al., 2020; Gose et al., 2018; Dean and Bhushan, 2010; García-Mayoral and Jiménez, 2011; Bidkar et al., 2014). While results are promising, challenges arise in full scale applications of these methods in ship hulls with regards to their durability and robustness over prolonged exposure periods and in high Reynolds number flows. Alternatively, active methods include polymer (Winkel et al., 2009; Elbing et al., 2013b) or air injection (air lubrication, Ceccio 2010) to modify the turbulent boundary layer (TBL). Furthermore, there is the possibility of combining active and passive methods, primarily to augment the efficiency of active ones (Fukuda et al., 2000; Peifer et al., 2020; Du et al., 2017). A more detailed overview of active and passive drag reduction methods can be found in Perlin et al. (2016).

A variety of different studies have showcased the potential of air lubrication systems. Cost benefit analyses have shown net power savings as high as 20% with corresponding reductions in emissions (Mäkiharju et al., 2012; Kim and Steen, 2023). Furthermore, net power savings

* Corresponding author.
E-mail addresses: M.Nikolaidou@tudelft.nl (L. Nikolaidou), a.laskari@tudelft.nl (A. Laskari), t.v.terwisga@marin.nl (T. van Terwisga), c.poelma@tudelft.nl (C. Poelma).

https://doi.org/10.1016/j.ijmultiphaseflow.2024.104948
Received 3 January 2024; Received in revised form 5 June 2024; Accepted 28 July 2024
Available online 31 July 2024

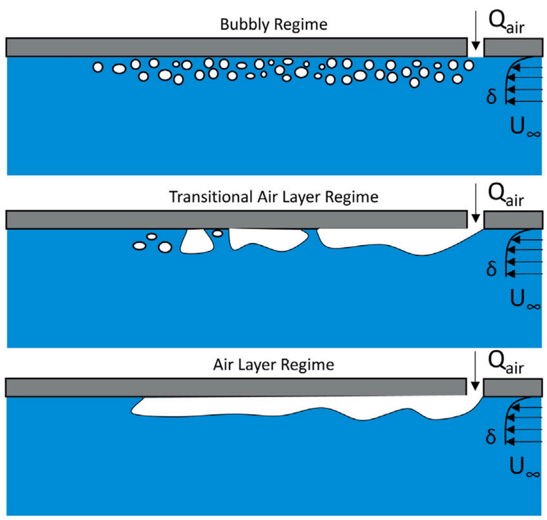

Fig. 1. Schematic representation of the different air phase regimes. From top to bottom: bubbly regime, transitional air layer regime, and air layer regime. Q_{air} increases from to top to bottom. Flow is from right to left.

of 4%–12% have been estimated based on sea trials under different sea conditions and ship types (Hoang et al., 2009; Mizokami et al., 2010; Fitzpatrick et al., 2017; Silberschmidt et al., 2016). In parallel with sea trials, towing tank experiments with model ships (Jang et al., 2014; Wang et al., 2020; Hao et al., 2019; Zverkhovskyi, 2014) and flat plate experiments in water tunnel facilities (Elbing et al., 2008; Barbaca et al., 2017; Zverkhovskyi, 2014) have been performed in order to provide insight in the governing mechanisms in drag reduction by air lubrication and to further improve the system efficiency.

In most of these studies, a cavitator or a backward-facing step (BFS) is used upstream of the air injection (Elbing et al., 2013a; Zverkhovskyi, 2014; Kim and Moin, 2010; Barbaca et al., 2017; Qin et al., 2019; Charruault et al., 2018; Hao et al., 2019; Lay et al., 2010; Peifer et al., 2020). The presence of this cavitator helps the creation of the air layer (commonly referred to as air cavity) and enhances its stability. However, this configuration demands a hull modification on existing ships, imposing practical obstacles to the implementation of such method. Furthermore, a cavitator or BFS can also increase drag in the hull in the absence of active air injection. Another option is the introduction of an air layer in the spatially developing TBL through a slot without the use of such inserts. Despite the practical advantages, this configuration is much less researched (Elbing et al., 2008; Jang et al., 2014; Sanders et al., 2006).

In this configuration, three different air phase regimes are commonly observed (Fig. 1). More specifically, for a constant liquid freestream velocity U_∞, increasing the air flow rate Q_{air} will consecutively lead to the bubbly regime (BR), characterized by the presence of dispersed bubbles in the flow, the transitional air layer regime (TALR), where alternating regions of bubbles and segments of air layer are present, and the air layer regime (ALR) where a continuous air layer is formed. Earlier studies focused on the bubbly regime, and more specifically on the effect of microbubbles on drag reduction, building upon the successful drag reduction experiments conducted by McCormick and Bhattacharyya (1973). Subsequent experiments within the BR (Madavan et al., 1984, 1985; Harleman et al., 2011) unveiled its limitations pertaining to the persistence of drag reduction away from the injection location and the necessary size of drag reducing bubbles. With regards to the bubble size, Verschoof et al. (2016), Lu et al. (2005) and Kim et al. (2021) highlighted the importance of bubble deformability, expressed by the Weber number, to achieve drag reduction. Murai (2014) offers a review on bubbly drag reduction. On the contrary, ALR does not suffer from the aforementioned limitations and so later studies have focused on that, showing that it is the most efficient in terms of drag reduction (Zverkhovskyi, 2014; Elbing et al., 2008). However, the sea state, trim and motion of the ship, the flow field around the hull, piping losses, and other factors significantly enhance the possibility that the air layer will not remain undisturbed and it will break into smaller segments (Mäkiharju et al., 2012). As such, a transitional (TALR), rather than an air layer regime is expected.

The first study to report TALR and the onset of ALR was Elbing et al. (2008). In this work, large scale experiments ($Re_x \approx 12 - 216 \times 10^6$) were performed in the US Navy's William B. Morgan Large Cavitation Channel (LCC). Drag reduction was achieved by injecting air from a slot through the top wall of a nearly zero-pressure-gradient TBL that formed on a flat plate test model. A large range of freestream velocities and air flow rates were tested, resulting in the different air phase regimes. According to the definitions introduced therein, once a drag reduction of 20% is achieved TALR is reached, while a drag reduction larger than 80% marks ALR. The associated air flow rates needed are defined as *transitional* air flow rate Q_{trans} and *critical* air flow rate Q_{crit}, respectively. The aforementioned definition of the regimes provided a way to define each regime, but required drag force measurements. In an attempt to step away from a definition coupled with the resultant drag reduction, Elbing et al. (2008) also introduced the critical nominal air thickness:

$$t_{\alpha,crit} = \frac{Q_\alpha}{BU_\infty} \tag{1}$$

with Q_α the critical air flow rate, B the injector span and U_∞ the liquid freestream velocity. The subscript α denotes that the parameter refers to a property of the air layer. According to their test cases a $t_\alpha > 4 - 8$ mm (depending on U_∞) was required to establish an air layer. This parameter, made dimensionless using the injection area rather than the injector's span was first used by Madavan et al. (1984) to scale bubbly drag reduction. In the study of Jang et al. (2014) an air layer was created experimentally below a long flat plate and local sensors were used to measure the drag. Following the definitions of Elbing et al. (2008), they found that a $t_{\alpha,crit}$ of 8.5 mm was needed to establish an air layer. That is however larger than the predicted one by Elbing et al. (2008) (about 4 mm) for the same velocity and a similar air injector geometry.

Another study classifying the different regimes is the work of Qin et al. (2019). While Elbing et al. (2008) focused on the scaling of BR and ALR drag reduction, Qin et al. (2019) included information on the air phase characteristics and focused on the air leakage mechanisms; they also made use of a cavitator prior to air injection, in contrast to Elbing et al. (2008). In their work, an air cavity was created underneath a flat plate in a water tunnel. Different air cavity regimes were created under various liquid freestream velocities U_∞ ($Re_x \approx 0.325 - 1.3 \times 10^6$) and Q_{air}. Based on the morphology of each regime (qualitative information from high speed imaging) and on the air discharge pattern they classified the air phase regimes. The authors found BR (referred to as 'foamy cavity regime'), a transitional cavity, an open cavity and a two-branch cavity. The transition from one regime to another was explained based on the gas entrainment mechanisms, using the shear layer as control volume for gas flux balances.

Apart from an earlier focus on BR and studies on regime transitions, more recently the ALR and its sensitivity to inflow conditions has also garnered some attention. First, the effect of the freestream velocity U_∞ on the air layer morphology (length and thickness) will be discussed, followed by the effect of the incoming TBL thickness δ. The former one is important because it directly impacts drag reduction. More specifically, a longer air layer would result in a larger non-wetted area and thus more drag reduction. In addition, a thicker air layer would be harder to break due incoming TBL induced perturbations in the air–water interface. Understanding and quantifying both effects on the air layer is critical in scaling lab results to full scale ones. As such, this is one of the goals of the present study. It must be noted that there are no studies (as far as we are aware) quantifying the air layer morphology in the absence of a BFS upstream of the injection position, so all the studies discussed next include a BFS or cavitator upstream of the air injection, while the terms air cavity and air layer will be used interchangeably.

The effect of U_∞ on ALR was investigated in the study of Zverkhovskyi (2014). An increase in the air cavity length with increasing U_∞ was observed. The maximum air cavity length (for a specific U_∞) matched reasonably well for a variety of cavitator heights with half the gravity wavelength predicted by the dispersion relation based on potential flow theory (see Butuzov 1966, 1967 for the theoretical analysis). Similar observations were also reported in Qin et al. (2019). An increase of U_∞ resulted in an increase of the fully developed air cavity length, which matched reasonably well with half a gravity wavelength for lower Froude numbers (lower freestream velocities). A deviation was observed for larger Froude numbers, where shallow water effects and longer cavity lengths are present. In contrast to the results from Zverkhovskyi (2014) and Qin et al. (2019), an increase in U_∞ led to a *shorter* air cavity in the study of Pearce et al. (2015); no comparison with half a gravity wavelength was performed and it is not clear if the maximum air cavity length (for a specific U_∞) was reached in their experiments.

Apart from the effect of freestream velocity, past studies, investigated the effect of the incoming liquid TBL thickness on ALR, in different ways depending on the capabilities of the experimental facilities used. In the study of Zverkhovskyi (2014), the incoming liquid TBL thickness was varied via changing the air injection position. Only marginal differences in the resulting air layer thickness and length were observed, although stronger small scale waves were observed at the air–water interface for larger development lengths; however, no detailed study of the liquid flow field around the layer was performed. Similar observations were also noted in the study of Pearce et al. (2015). In this study the incoming liquid TBL thickness was varied by artificial thickening (or thinning) at the water tunnel inlet. A shorter air cavity length was observed for a larger incoming TBL thickness. The authors attributed the latter to the lower kinetic energy at the air–water interface, although no turbulence profile measurements were performed to further support this assumption. In addition, the studies of Barbaca et al. (2017, 2018) showed that the air cavity length decreased with increasing TBL thickness. They attributed this effect to a less pronounced blockage effect (as described by Brennen 2014) for a thicker incoming TBL and a thinner air cavity. It should be noted here again that the previous observations on U_∞ and thickness effects on the air layer geometry were explored in BFS configurations. Nonetheless, experiments without BFS in the bubble drag reduction regime (BR) showed that a doubling of the boundary layer thickness at the injection position had a negligible effect on the resulting drag (Elbing et al., 2008); this effect was, however, not investigated for the case of an air layer. The only incoming flow effect on the air layer regime discussed in that study was the negative influence of upstream disturbances on achieving an ALR.

Apart from qualitative observations on the air–water interface perturbations found in literature, very few experimental studies are available on the effect of incoming flow conditions on the actual air layer thickness. This is possibly due to the difficulties that such a measurement entails. In the work of Elbing et al. (2013a), similar experiments as the work of Elbing et al. (2008) are performed, with the difference that a BFS is now added prior to the air injection point. Using electrical impedance point probes the authors measured the air void fraction in different vertical distances from the flat plate, in order to estimate the edge of the air phase, or actual ALR thickness, t_{air}. They observed a steep decrease in their signal for $t_{air} = (3/4) \times t_\alpha \approx 7$ mm, independent of downstream distance, indicating both an insensitivity to incoming TBL conditions and a lower actual ALR thickness than the nominal estimate. The latter could be due to the use of the liquid velocity U_∞ in the calculation of t_{air} instead of the velocity of the air phase. Regardless, these observations were available for a single U_∞, thus their universality could not be established. In contrast, a much lower t_{air} ($\approx$ 1 mm) was reported in the case of Elbing et al. (2008) in the absence of a BFS. Thus, the effect of TBL on t_{air}, as well as its relationship with t_α still remain unclear, especially in the absence of a BFS prior to air injection.

Based on the above, it is clear that effects of inflow conditions on the different air phase regime characteristics are still not well-established, even for configurations employing BFS, while they are completely lacking in the absence of such inserts. In this context, in the current study, we aim to investigate the effect of different incoming TBL conditions on both the regime transitions and their characteristics, with a focus on ALR, in configurations without a BFS.

The remainder of this paper is organized as follows: Section 2 describes the experimental setup and methods; Section 3 presents the results along with a discussion on the effect of incoming TBL flow conditions on the regime transitions and the air layer topology and Section 4 provides a summary of this work and the conclusions drawn from it.

2. Experimental setup and methods

In the following section the experimental setup is described. Two types of experiments are performed: velocity measurements using particle image velocimetry (PIV) for the liquid TBL and imaging for the air phase. First the experimental facility and setup considerations are presented followed by details on the PIV and imaging experiments.

The flow facility used for the study is the recirculating, closed-loop water tunnel at the Laboratory for Aero- and Hydrodynamics of Delft University of Technology. The test section of the tunnel has a cross-sectional area of 60 × 60 cm^2 and a length of 5 m. The maximum freestream velocity U_∞ is about 1 m/s. The open surface of the water tunnel is covered with two identical flat plates, each 2.485 m long, tightly placed one after the other. The water depth is d = 58 cm.

One of the plates is fitted with a slot type air injector, spanning the central 58 cm of the plate width. The gap width is 4 mm. Both plates are equipped with side fences to prevent the air from escaping through the sides. Compressed air is injected from the top side of the plate through two manifolds and dispersed over the width of the slot (schematically shown in Fig. 2). In that way, the compressed air is not directly introduced to the liquid flow, but firstly dispersed over a 210 mm × 2 mm × 580 mm chamber. The air injector geometry is inspired by the air injector geometry in the work of Zverkhovskyi (2014), only slightly modified to ensure that the air is distributed equally over the width of the current facility. The air flow rate, Q_{air}, is manually controlled with a valve and measured with a rotameter and varied from 2.5 l/min to 52 l/min (accuracy of 1 l/min).

The flow is tripped with a 0.5 mm thick zig-zag trip located 8 cm downstream of the start of the first plate to ensure a turbulent boundary layer. The corresponding Re_θ at the tripping location varied from 150 to 190 based on the Blasius's solution for a laminar boundary layer. As indicated by previous measurements in this water tunnel (Harleman et al., 2011), the boundary layer development starts already in the contraction region prior to the test section (approximately 1 m upstream). This is also taken into account in the current measurements.

In order to achieve 4 different incoming TBL thicknesses prior to the air injection, the air injector position is varied with respect to the start of the test section. This is achieved via flipping the plate housing the air injector (resulting in development lengths x_2&x_4) and via changing the sequence of the two flat plates covering the water tunnel (resulting in development lengths x_1&x_3). In Fig. 2a all four positions are shown and the air layer is shown in position x_1 for reference. Due to modifications needed when moving the air injector location to these positions, the final gap width of the injector ended up varying slightly. As such, and to ensure consistent comparisons, in what follows we will compare effects

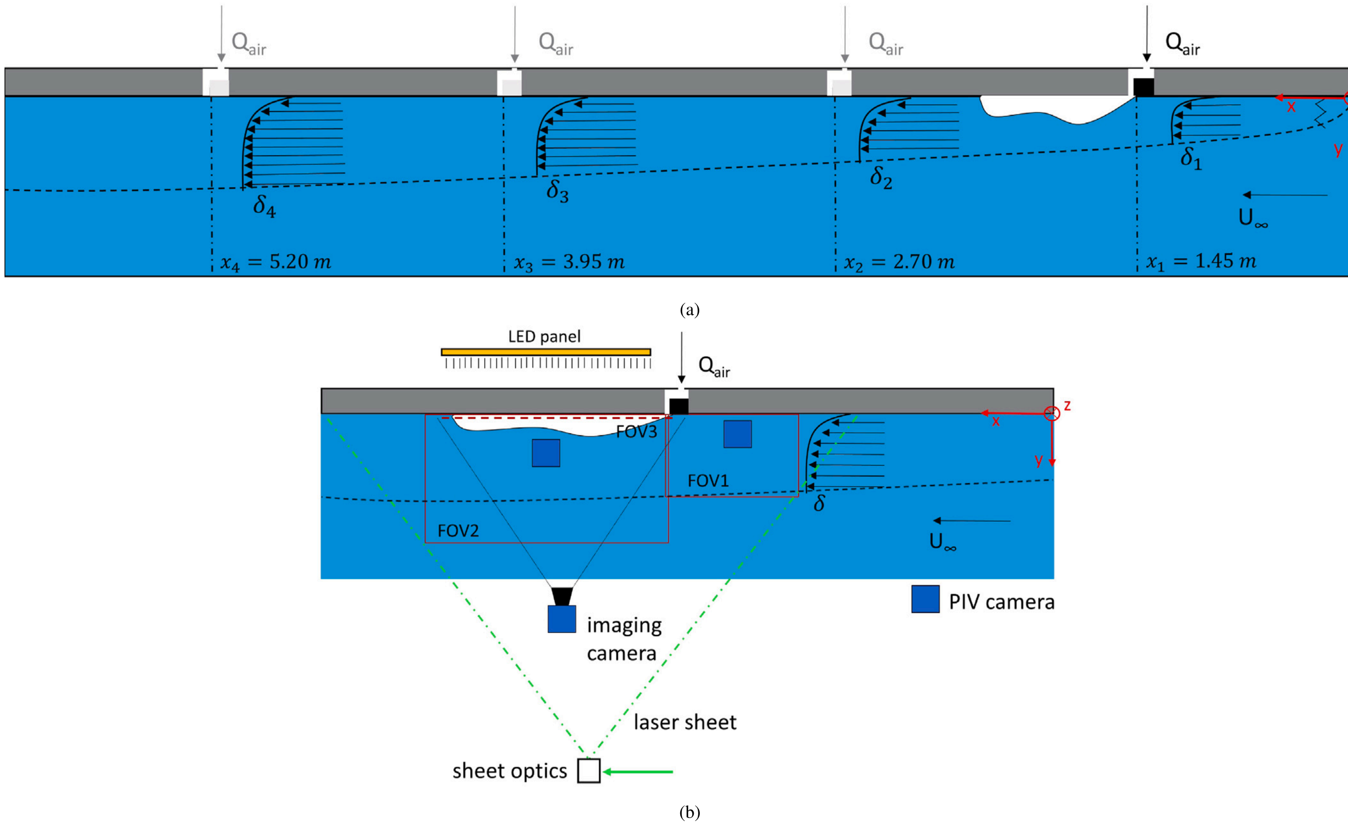

Fig. 2. (a) Schematic of the water tunnel with the four different air injection positions. The air layer is sketched in position 1 for reference. The other three injection positions are indicated in gray. In each experiment the injector is moved such that the remainder of the plate is flat in all other positions. (b) Schematic overview of the different FOVs. FOV1 & FOV2 are in x-y plane while FOV3 is in y-z plane. Flow is from right to left.

Table 1
Summary of experimental conditions.

Injection position	Development length x (m)	Freestream velocity U_∞ (m/s)	Q_{air} (l/min) PIV	Q_{air} (l/min) imaging	Model injector
1	$x_1 = 1.45$	0.68 0.77 0.86 0.92	0 & 41	5–41	A
2	$x_2 = 2.70$	0.70 0.79 0.87 0.95	0 & 52	5–52	B
3	$x_3 = 3.95$	0.71 0.80 0.89 0.96	0 & 41	5–41	A
4	$x_4 = 5.20$	0.72 0.81 0.90 0.97	0 & 52	5–52	B

of incoming TBL on positions x_1 and x_3 (model A), and positions x_2 and x_4 (model B).

For each of the four injection positions, four freestream velocities are tested, ranging from U_∞ = 0.68 m/s to 0.96 m/s with a Reynolds number based on the water depth, Re_d ($= U_\infty d/\nu$) ranging from 3.94×10^5 to 5.45×10^5. For all cases the water depth based Froude number Fr_d ($= U_\infty/\sqrt{gd}$) remained below one (0.29 – 0.4). While all the tested freestream velocities and air injector positions are the same for both PIV and imaging, the former was only performed for a single air flow rate while the latter, for a range of air flow rates capturing BR, TALR and ALR. Table 1 provides a summary of the tested conditions.

In each position, firstly velocity measurements without air are conducted ('air off' case), followed by measurements with an air layer present ('air on' case). More specifically, the air flow rate is set to a constant value (see Table 1 for specific values during each test) corresponding to the stable air layer regime (Nikolaidou et al., 2021). As noted by other researchers (Yoon et al., 2020), velocity measurements using PIV in the transitional or bubbly regime are more challenging due to the presence of dispersed bubbles. In both cases (with and without air), FOV1 (250 × 167 mm^2) captures the incoming boundary layer prior to the air injector and FOV2 (468 × 314 mm^2) captures simultaneously either the developing boundary layer after the air injector ('air off' case) or its development around the air layer ('air on' case), with planar (2D-2C) PIV (Fig. 2b). The aforementioned dimensions for the FOV correspond to position x_2, but similar values were also achieved for the other positions. For FOV1 and FOV2, two high-resolution LaVision LX pro (16 MegaPixel, 12-bit) cameras are used. The acquisition frequency is 0.7 Hz and 1600–2500 statistically independent images are recorded for each FOV. The laser sheet is introduced from the bottom creating a thin sheet (∼ 1 mm) in a streamwise-wall-normal (x-y) plane at the tunnel's mid-span. Hollow glass spheres of mean diameter of 11 μm are used as tracer particles. The optical magnification is approximately 10.33 px/mm for the larger (downstream) FOV2 and 19.38 px/mm for the smaller (upstream) FOV1. Raw images are processed with DaVis 8.4 (LaVision GmbH) using a multi-pass cross-correlation algorithm with initial (final) window size of 48 × 48 (24 × 24) pixels and 50% overlap. That results in a spatial resolution of the velocity field (based on the final interrogation window size) of approximately dx = 1.24 mm and dx = 2.32 mm for FOV1 and FOV2 respectively. Again the aforementioned values correspond to the measurements at position x_2. Spurious vector elimination is performed via universal outlier detection (Westerweel and Scarano, 2005). This is followed by filtering the velocities vectors with more than 3 times the (local) standard deviation.

Following the velocity measurements, an imaging camera is used in a down-up configuration to capture the different air phase regimes. It

Table 2
Summary of the incoming TBL properties for the different injection positions. Data come from the test condition without air.

Injection position	x (m)	U_∞ (m/s)	$Re_x \times 10^6$	Re_θ	Re_τ	θ (mm)	δ (mm)	Model injector
1	1.45	0.68	0.99	2996	1441	4.4	51	A
1	1.45	0.77	1.11	3688	1634	4.8	52	A
1	1.45	0.86	1.24	3606	1214	4.2	37	A
1	1.45	0.92	1.33	4785	1991	5.2	54	A
2	2.70	0.70	1.89	4894	2593	7.0	93	B
2	2.70	0.79	2.12	5653	3059	7.2	99	B
2	2.70	0.87	2.36	7343	3454	8.4	104	B
2	2.70	0.95	2.56	8896	3898	9.4	110	B
3	3.95	0.71	2.80	5315	3314	7.5	118	A
3	3.95	0.80	3.15	7423	4439	9.3	142	A
3	3.95	0.89	3.52	7220	3198	8.1	95	A
3	3.95	0.96	3.81	7999	3444	8.3	96	A
4	5.20	0.72	3.72	9512	4475	13.3	162	B
4	5.20	0.81	4.23	13 263	4848	16.3	169	B
4	5.20	0.90	4.70	10 935	4806	12.1	144	B
4	5.20	0.97	5.02	11 108	5298	11.5	147	B

must be stressed that the PIV and imaging are not performed simultaneously but rather one after the other to make sure that no modifications take place in between the two experimental campaigns. In each of the four air injection positions and for four different freestream velocities (Table 1), the air flow rate is varied from 2.5 l/min to 52 l/min resulting in images of different air phase regimes. A LaVision Imager sCMOS CLHS camera fitted with a 24 mm lens is used to image the air phase regimes in a streamwise–spanwise (x-z) plane while an LED panel provided background illumination. Image acquisition is done using DaVis 10.4, at 2 Hz allowing statistically independent snapshots. The field of view is approximately 700 × 600 mm^2 and the magnification approximately 3.6 px/mm in both directions.

3. Results & discussion

3.1. Characterization of incoming TBL

First a characterization of the liquid incoming TBL is performed for the four different air injection positions and freestream velocities. Mean velocity profiles were computed both in the absence of an air layer (unperturbed TBL) and with an air layer present. Based on a previous study (Anand, 2021), the presence of the air layer is expected to also have an effect on the *upstream* TBL and more specifically to impose an adverse pressure gradient to the liquid TBL upstream of the air injection position. Given that the freestream turbulence intensity (about 2.5% in our case) already influences the developing TBL along the top wall of the water tunnel (Jooss et al., 2021), pressure gradients due to the presence of the air layer would further complicate the characterization of the baseline TBL. It is therefore decided to use the unperturbed TBL as our reference case when assessing the influence of the upstream flow conditions. That being said, the influence of the air layer on the incoming TBL is also quantified in Section 3.2 and a comparison is made with the unperturbed case.

For all positions except x_4, FOV1 ('air off' case) was used for characterization of the upstream flow conditions (spatially averaged mean velocity profiles in the absence of strong streamwise pressure gradients), capturing about 1.5δ in y. For position x_4 however, the field of view was smaller than the TBL thickness (FOV1$< \delta$) and as such the velocity fields from FOV2 were used instead (the streamwise distance between the two locations in the absence of air leads to negligible additional boundary layer development).

The boundary layer thickness is defined as the wall normal distance where the velocity is 99% of the freestream velocity. U_∞ and δ were then determined iteratively with U_∞ defined as the mean of all data points with $y > \delta$. The friction velocity was determined with the Clauser chart method (Clauser, 1956). Fig. 3 shows the inner scaled mean streamwise velocity profile as a function of non-dimensional wall units y^+ compared with Laser Doppler Anemometry (LDA) data from De Graaff and Eaton (2000) at a similar Reynolds number. The computed freestream velocities indicated a 4% increase between locations x_1 and x_4 due to BL growth in the absence of a sloping bottom wall. Table 2 provides a summary of the TBL properties for all cases considered. As expected, the TBL thickness is increasing along the length of the water tunnel for the four positions considered. Comparing positions x_1 and x_3, it can be observed that δ is doubled but in between x_2 and x_4 δ is only 50% higher, even though they are the same distance apart. This can be attributed to high turbulence intensity and other tunnel imperfections (slight misalignment of components due to the long facility length). As such, and given the aforementioned changes in the injector geometry, effects of increasing δ will be considered separately for model A (x_1&x_3) and model B (x_2&x_4): δ is always thicker in the second position for both models but not necessary of the same order increase. The velocity induced δ variations for the same injection position are higher (5%–20%) than expected (≈ 4%), yet they are much lower than those due to the change in development length and are thus not considered relevant in this parameter study. As a result, the incoming TBL thickness δ and development length x will be used interchangeably to refer to the various locations/conditions.

In the real case scenario of a developing TBL below the hull of a ship, a thick TBL is expected just upstream of the air injection. Although this depends on the position of the air injector along the hull, a Reynolds number based on the downstream distance Re_x of the order of 10^9 and a thick boundary layer (≈1–2 m) is expected (small t_{air}/δ) in general. The potential importance of the ratio t_{air}/δ on the air phase regimes has, however, not been previously investigated. In the current study, and given a maximum t_{air} ≈15 mm, the incoming TBL would yield a ratio of $t_{air}/\delta \approx 0.1$, in the case of the larger development length (x_4). That would indicate that the air layer extends into the log region. On the other hand, a ratio of 0.3 in the case of the shorter development length (x_1) would position the air layer boundary in the lower wake region. In the studies performed in the LCC (Elbing et al., 2008, 2013a) a much smaller t_{air}/δ is present (0.078 for Elbing et al., 2013a and around 0.012 ($y^+ = 222$) for Elbing et al., 2008). In the study of Zverkhovskyi (2014) the ratio is 2.1. Barbaca et al. (2018) do not report a t_{air}, but the air layer thickness is of the order of the BFS height h, yielding a ratio in the range of 0.13 – 0.52, similar to the current study. Reflecting on this ratio is important because it leads to different turbulent scale size and spacing in the spanwise direction (Kevin et al., 2019; Dennis and Nickels, 2011; de Silva et al., 2018) of the liquid incoming flow, which will affect the air layer, especially in the absence of a BFS upstream of the air injection.

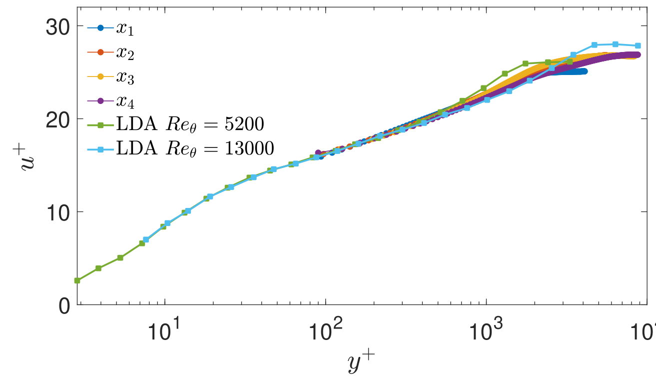

Fig. 3. Double mean streamwise velocity profiles of the incoming boundary layer for the four different air injection positions in the case of the higher streamwise velocity ($U_\infty = 0.92 - 0.97$ m/s) compared with LDA data from De Graaff and Eaton (2000).

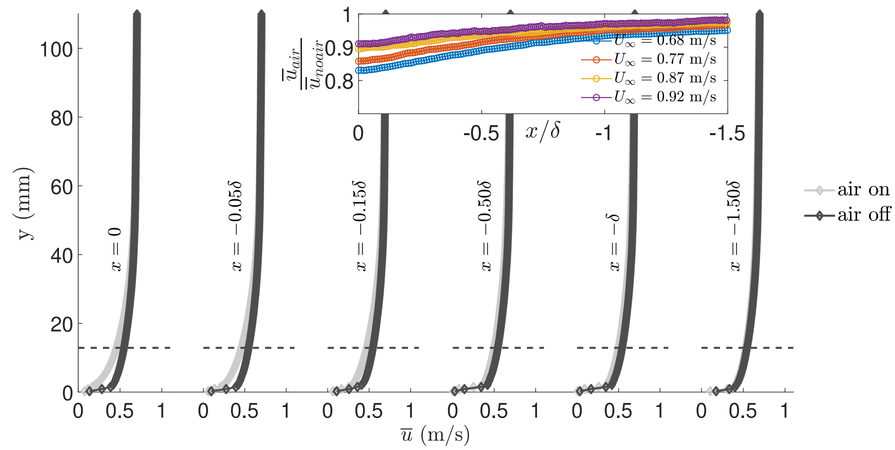

Fig. 4. Mean streamwise velocity profiles of the incoming TBL with and without the air layer present at injection position x_2 and $U_\infty = 0.70$ m/s. The air layer starts at $x = 0$ and the most upstream station is at $x = -189$ mm. The dashed line indicates the air layer thickness. Insert: streamwise variation of the ratio of the mean streamwise velocity with and without air at $y = t_{air}$ where t_{air} is the measured air layer thickness. Flow is from left to right.

3.2. Influence of the air layer on the incoming TBL

The incoming flow affects the air phase dynamics and in turn the incoming flow is affected by the air layer/bubbly flow. It is then important to assess the influence of the air layer on the incoming TBL and make use of the actual incoming flow conditions in our future analysis: the local flow parameters (e.g. the velocity in the vicinity of the air layer/bubbly flow rather than the freestream one) of the incoming TBL upstream of the injection position.

As mentioned in Section 2, the incoming TBL is measured with and without an air layer present for flow conditions summarized in Table 1. A comparison of the streamwise time-averaged velocity with and without the air layer present is presented in Fig. 4 for position x_2 and a freestream velocity of $U_\infty = 0.70$ m/s. As can be seen, the upstream influence of the air layer on the incoming TBL extends to about $x = -\delta$ upstream of the air injection ($x = 0$). This is equivalent to $x = -0.62L_{air}$, where L_{air} is the mean air layer length. In addition, at all stations, the influence of the air layer in the wall-normal direction extends up to the outer region, at around $y = 0.5\delta$. For the same Re_x, similar behavior is observed in Anand (2021) (influence up to $y = 0.4\delta$). An increase of Re_x, either due to a larger incoming development length x or a higher U_∞, results in a less pronounced effect of the air layer on the incoming TBL. This is illustrated in the insert of Fig. 4, where the ratio of the mean streamwise velocity with and without air over the streamwise development length x is shown for different U_∞ at position x_2. It is estimated that for position x_4 and the larger U_∞ tested, the upstream influence of the air layer on the incoming TBL is only $x = -(0.1 - 0.2)\delta$ corresponding to 4%–8% L_{air}. On the other extreme, for the lower Re_x tested at position x_1, the air layer influences the incoming TBL up to $x = -2.5\delta$ corresponding to 0.75% L_{air}.

3.3. Characterization of BR, TALR and ALR under different incoming flow conditions

Following the characterization of the incoming liquid TBL, a characterization of the air phase is presented in this section. Three very distinct air phase regimes were observed for different Q_{air} and U_∞. The bubbly regime (BR), the transitional air layer regime (TALR), and finally the air layer regime (ALR). In Fig. 5, characteristic instantaneous images of these are shown for the four different freestream velocities U_∞ tested, for four different air flow rates Q_{air}, and for the incoming development length x_3. In addition, in order to support the qualitative information presented in Fig. 5, the percentage of non-wetted area A_{nw} versus Q_{air} is presented in Fig. 6. The former is defined as:

$$A_{nw} = \frac{A_{air}}{A_{total}} \times 100 \tag{2}$$

where A_{air} is the flat plate area occupied by air and A_{total} is the total flat plate area. To calculate A_{nw}, an image processing algorithm in MATLAB is employed. More specifically, for each instantaneous grayscale image (Fig. 5), small structures are first removed by Gaussian filtering, followed by background normalization. Then the images are binarized based on the gradient magnitude. Finally, morphological closing (dilation followed by erosion) is performed and the remaining bubbles/air patches are filled. The average value of A_{nw} for a specific U_∞ - Q_{air} pair and its standard deviation is then calculated.

Bubbly regime

For a low air flow rate (Q_{air} = 10.3 l/min), dispersed bubbles are present in the flow (marked as BR in Fig. 5). In this regime the bubble size d_b ranges from millimeters to centimeters (see also supplementary video S1), but individual bubbles may coalesce to form larger ones far downstream from the air injector. This regime is morphologically similar to the bubbly regime reported by Elbing et al. (2008) and the foamy cavity regime reported by Qin et al. (2019) for the lower tested Q_{air}. In those studies, bubbles are located in various wall-parallel planes as a result of the recirculating flow behind the BFS but in our cases, a single bubbly plane is formed very close to the flat plate (in all cases $d_b < \delta$, see also supplementary video S1). For the same Q_{air}, increasing U_∞ results in smaller bubbles as can be seen in Fig. 5 for Q_{air} = 10.3 l/min and increasing U_∞.

Transitional air layer regime

Further increasing Q_{air} results in progressively larger bubbles leading to an increase in A_{nw} and a decrease of the bubble's perimeter (Fig. 6). However at a certain air flow rate ($Q_{air} > Q_{trans}$), once the transitional air layer regime is reached, bubbles, air patches and parts of an air layer are present in the flow. This is the least researched regime but yet quite important because, in full scale ship conditions, the air layer will break due to various parameters. In this regime, A_{nw} steeply increases with increasing Q_{air} (Fig. 6). In essence, a small change in Q_{air} could lead to either the bubbly or the air layer regime. It is then expected that the inflow conditions are very important since they could provide either the conditions to promote transition to ALR or impose bubble break up (BR). Large standard deviations (due to the instantaneous variation) of A_{nw} are evident from Fig. 6 indicating the highly dynamic character of this air phase (see also supplementary video S2). Characteristic images of this regime are marked with TALR in Fig. 5 for clarity. It can be seen from Fig. 6 that for $U_\infty = 0.80$ m/s and $U_\infty = 0.89$ m/s, the A_{nw} peaks at the TALR rather than the ALR. It is not clear however if this highly dynamic regime (coupled with high A_{nw}) results in high drag reduction as well.

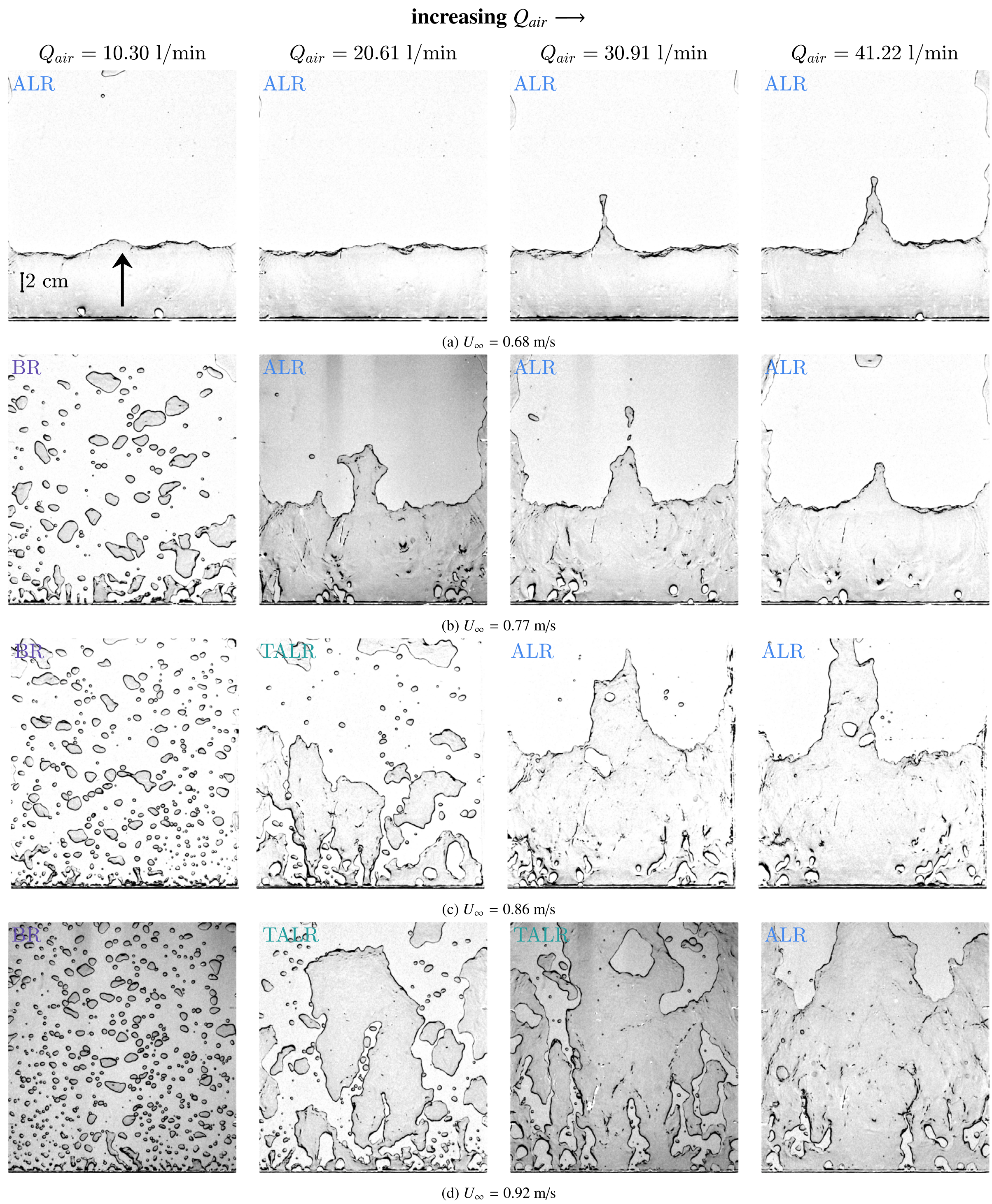

Fig. 5. Characteristic images of the different air phase regimes for the freestream velocities tested (injection position x_3). The air flow rate increases from left to right. Bubbly, transitional and air layer regimes are marked for clarity. In all images the lighter background indicates liquid and the darker color the air phase. Each row shares the same freestream velocity and each column the same air flow rate. Flow direction is from down up.

Air layer regime

Further increasing the air flow rate ($Q_{air} > Q_{crit}$) results in the air layer regime (characteristic images of this regime are marked as ALR in Fig. 5). In this regime, an air cavity, with a thickness of ≈ 1 cm, clearly separates the solid wall from the liquid phase. In the case of $U_\infty = 0.71$ m/s and $U_\infty = 0.80$ m/s the air cavity resembles a two branch cavity, similar to the two branch cavity (TBC) cavity observed by Qin et al. (2019). Two elongated air branches (one on each side of the air layer) are always present while there are some instances that air is discharged from a third middle branch. For the higher velocities $U_\infty = 0.89$ m/s and $U_\infty = 0.96$ m/s a three-branch air cavity is observed (Fig. 5(d), see also supplementary video S3). This was not observed by Qin et al. (2019), in a narrower facility than the one used for the current experiments. While investigating the air discharge mechanisms is out of the scope of this study, it is important to note that, in all cases, the air leaks from the cavity through bubble pinch-off at the end of the branches due to the presence of small surface waves at the liquid–air interface. This is similar to the instability mechanism for a two branch

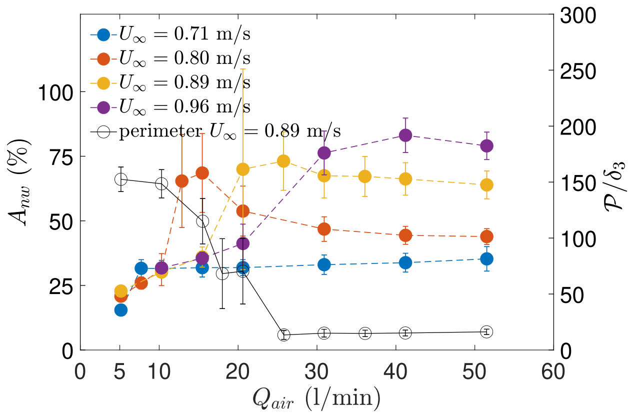

Fig. 6. Percentage of non-wetted area A_{nw} % for various air flow rates and freestream velocities. Results are shown for air injection position x_3 (model A). Error bars indicate the standard deviation due to the instantaneous variation of A_{nw}. For $U_\infty = 0.89$ m/s the normalized perimeter of the air phase items is also shown.

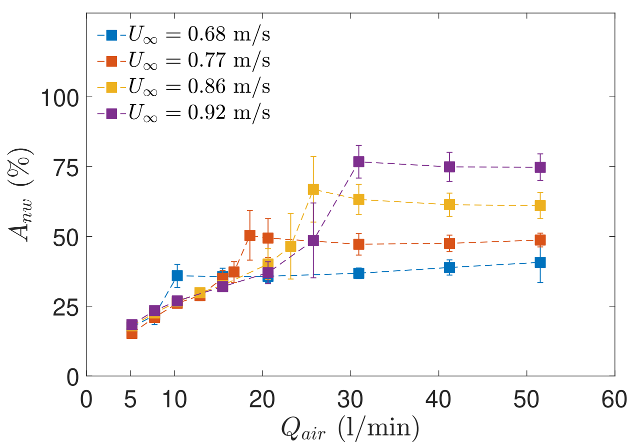

Fig. 7. Percentage of non-wetted area A_{nw} % for various air flow rates and freestream velocities. Results are shown for air injection position x_1 ($\delta_1 < \delta_3$, model A). Error bars indicate the standard deviation due to the instantaneous variation of A_{nw}.

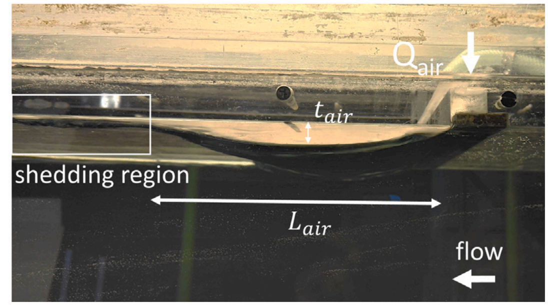

Fig. 8. Side view of the air layer. Air layer thickness t_{air} denotes the maximum thickness at the apex of the cavity. Air layer length L_{air} corresponds to the spanwise uniform part of the air layer (excluding the shedding region).

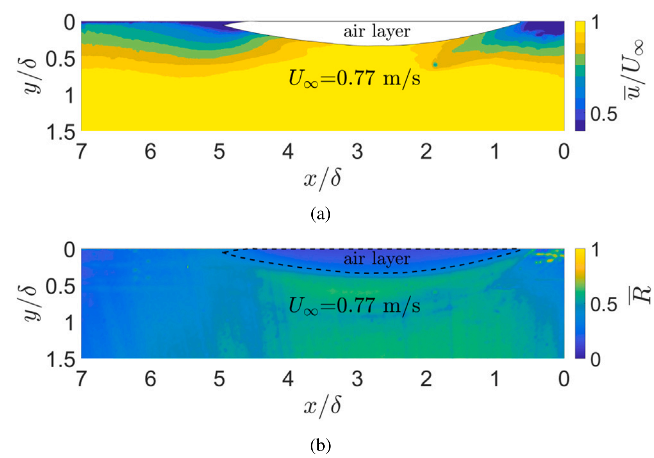

Fig. 9. (a) Mean streamwise velocity field around the air layer (air layer marked in white color) and (b) mean correlation map used to extract the air layer thickness. Black dashed line denotes the air–water interface.

cavity mentioned by Qin et al. (2019). Once the air layer is formed, further increasing Q_{air} has no significant effect on the morphology of the air layer, apart from a delay in the air layer break up close to the air injector (wetted pockets, seen in Fig. 5). This is also evident in Fig. 6 where A_{nw} seems unaffected by the increase of Q_{air} in ALR.

The effect of U_∞ on the air layer characteristics can be qualitatively seen in Fig. 5. For the same air flow rate Q_{air} = 20.61 l/min, a TALR is present for U_∞ = 0.86 m/s, while for U_∞ = 0.77 m/s we observe an ALR. This is also demonstrated in Fig. 6, where there is an evident shift of the curves to the right, corresponding to higher Q_{air}. Thus, increasing U_∞ inhibits/delays the formation of a stable air layer. This will be further discussed in Section 3.5.

Incoming TBL thickness effect

In Fig. 7, A_{nw} in the case of a thinner incoming TBL (development length x_1) is shown. Qualitatively, Figs. 6 and 7 are similar, however relative less value peaks of A_{nw} are present in Fig. 7 indicating that fewer instances of TALR are present in this case. Similar behavior is observed for an increase in δ for the model B injector (not shown here).

3.4. Effect of incoming flow conditions on the air layer geometry

In this section the focus will be on the ALR and its geometrical characteristics under different incoming δ and U_∞. Given that the ALR is the most important regime in terms of drag reduction, it is useful to pay more attention to its characteristics. As discussed in , once the ALR is reached (for a specific δ - U_∞ pair), no significant morphological changes are observed, making ALR the most amenable to further quantitative analysis. In addition, there has not been a quantitative analysis of the ALR in a configuration without a BFS, leading to uncertainty regarding how these two configurations compare.

Regarding the ALR, it was already apparent from Section 3.3 that the morphology of the air layer differs with incoming flow conditions including the presence of a two or three branch cavity and the amount of wetting events near the air injector. Here, we will focus on the air length L_{air} and air layer thickness t_{air} for different U_∞ and incoming δ. These are expected to directly impact the stability of the air layer. In what follows, t_{air} is defined as the maximum thickness at the apex of the air cavity, while L_{air} is defined as the mean streamwise length of the spanwise homogeneous part of the air layer (excluding the branches in the shedding region). These definition are also shown in Fig. 8. The method used to calculate each of them will be also expanded upon.

3.4.1. Variation of t_{air} with incoming flow conditions

First, the air layer thickness t_{air} is discussed. As explained in Section 2, planar PIV was performed to measure the liquid velocity around the air layer. In the absence of seeding particles in the air phase, a noticeable decrease of the correlation value R of the particle image pairs was evident. The thickness t_{air} was then determined from the time averaged correlation value R of the particle image pairs. Subsequent appropriate thresholding using Otsu's method (Otsu, 1979) and image processing of the mean correlation maps, allowed the determination of

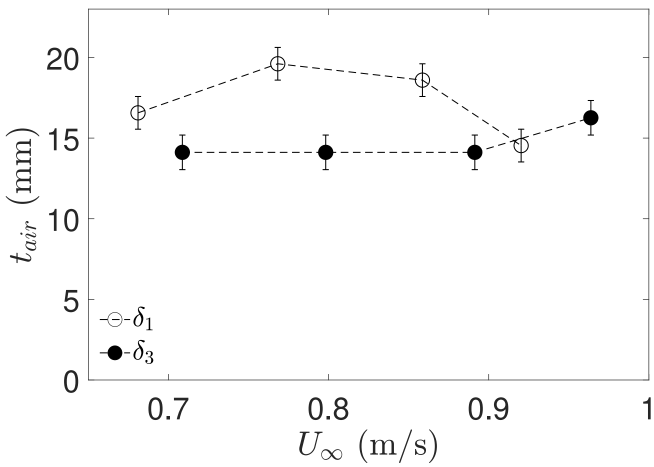

(a)

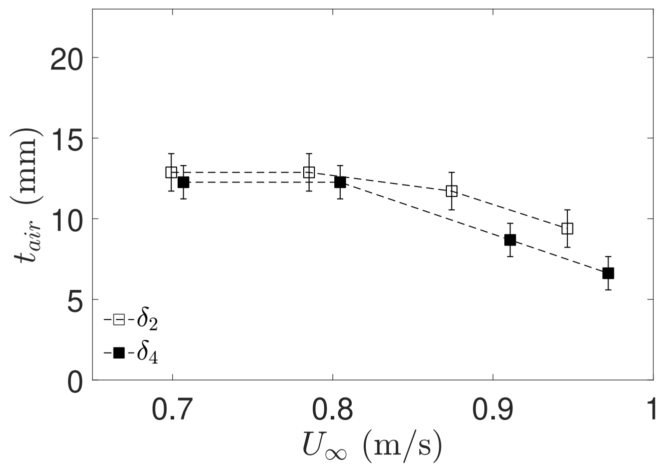

(b)

Fig. 10. Measured thickness t_{air} of the air layer for different freestream velocities for air injection positions (a) x_1 and x_3 (model A injector) and (b) x_2 and x_4 (model B injector).

the mean air water interface and its maximum thickness (at the apex of the concave interface, see also Fig. 8) for all conditions. Another way of determining the air layer thickness from PIV images was proposed by Anand (2021), where the air–water interface is estimated at each time instance, using the instantaneous instead of the time averaged correlation maps. Both methods yield similar results (< 1 mm difference). In Fig. 9(a), the mean streamwise velocity around the air layer is shown and the air layer shape is acquired from Fig. 9(b).

In Fig. 10, t_{air} with its uncertainty, is reported for different U_∞. By comparing the injection positions that share the same injector model we can also see the effect of incoming δ. It can be seen that for both model injectors, the thinner incoming TBL (δ_1 and δ_2) resulted in a larger t_{air} compared to the thicker one (δ_3 and δ_4). On one hand, the spatial resolution of the PIV (2 mm based on the final interrogation size — not taking into account the 50% overlap) was sufficient to estimate t_{air}, which is around 15 mm for the model A injector (Fig. 10(a)) and 10 mm for the model B injector (Fig. 10(b)). The difference is attributed to the smaller gap width of model injector B. It must be noted that it is the first time that the actual air layer thickness is measured in this configuration. On the other hand, the uncertainty level due to the detection method itself and the limitations of the experimental setup (reflections at the air water interface) make it difficult to determine a trend of t_{air} with the incoming TBL.

In the study of Elbing et al. (2013a), where a BFS was used prior to the air injection, the thickness of the air cavity was estimated to be $0.75t_a$. Following this definition in the current experiments, we would expect a t_{air} in the range of $\approx 1.5-2$ mm. However, the measured t_{air} is an order of magnitude thicker. The aforementioned discrepancy could be attributed to the Reynolds number difference between the current study and Elbing et al. (2013a) ($Re_\tau = 14140$). In any case, it seems that U_∞, B, and Q_{air} alone cannot predict t_{air}.

Since we have calculated t_{air} and the liquid incoming TBL thickness δ (Section 3.1), it is insightful to calculate the ratio of the two, in order to identify the expected characteristics of the local TBL structures in the vicinity of the air layer interface. In Fig. 11, the mean streamwise velocity profiles in different air injector positions are shown. The dashed lines indicate the ratio t_{air}/δ. This is plotted here for $U_\infty = 0.68$ m/s, but the rest of the velocities show a similar behavior. As can be seen, the air layer interface in position x_1 is in the wake region ($y/\delta \approx 0.3-0.4$), in x_2 and x_3 it is at the outer edge of the log region ($y/\delta \approx 0.12-0.14$) and in x_4 it is well within the log layer ($y/\delta \approx 0.06$). The associated velocity fluctuations of the incoming liquid TBL in these regions are known to differ in both amplitude and spanwise extent (Dennis and Nickels, 2011). In particular, for position x_1, velocity fluctuations close to the air liquid interface (wake region) would be wider in span, with lower amplitudes (leading to smaller variations of the instantaneous velocity from the local mean of that plane). On the other hand, as we move to position x_4, the incoming TBL is thicker, while the air layer thickness is approximately constant. As a result the spanwise fluctuations of the streamwise velocity are expected to be thinner and of higher amplitude (leading to larger variations of the instantaneous velocity around the local mean) in the vicinity of the air–water interface.

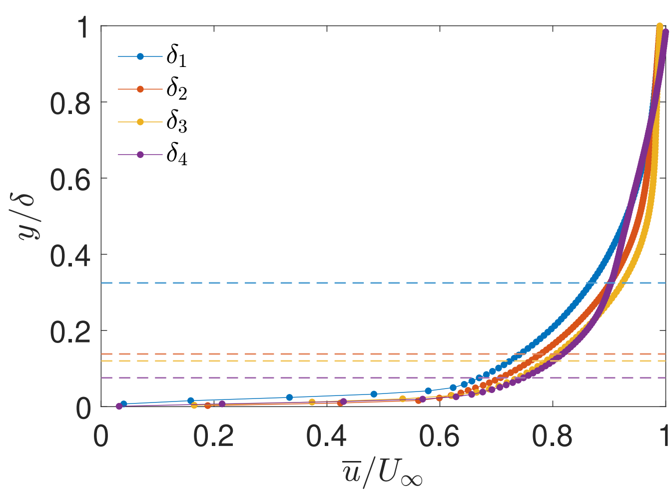

Fig. 11. Mean streamwise velocity profile normalized with the freestream velocity for different incoming TBL thicknesses (air injection positions) for the lower freestream velocity tested ($U_\infty = 0.68-0.72$ m/s). Dashed lines indicate t_{air}/δ.

3.4.2. Variation of L_{air} with incoming flow conditions

The air layer length L_{air} is directly estimated from the imaging camera which allows accurate determination. It could also be estimated from the mean correlation map of PIV images in a similar manner as t_{air} was determined. However, difficulties pertaining to the unsteady character of the closure region of the air layer made the detection of L_{air} through the PIV images challenging, especially for the higher U_∞. Characteristic images of the air layers are shown in Fig. 12 for the four different U_∞ tested and for two positions. Via image processing, the air layer closure line is first detected (blue line in Fig. 12). In line with other studies (Qin et al., 2019) L_{air} is defined as the shortest distance between the air injector and the location of the cavity closure line. In case of a thinner incoming TBL (Figs. 12(a)–12(d)), the air layer

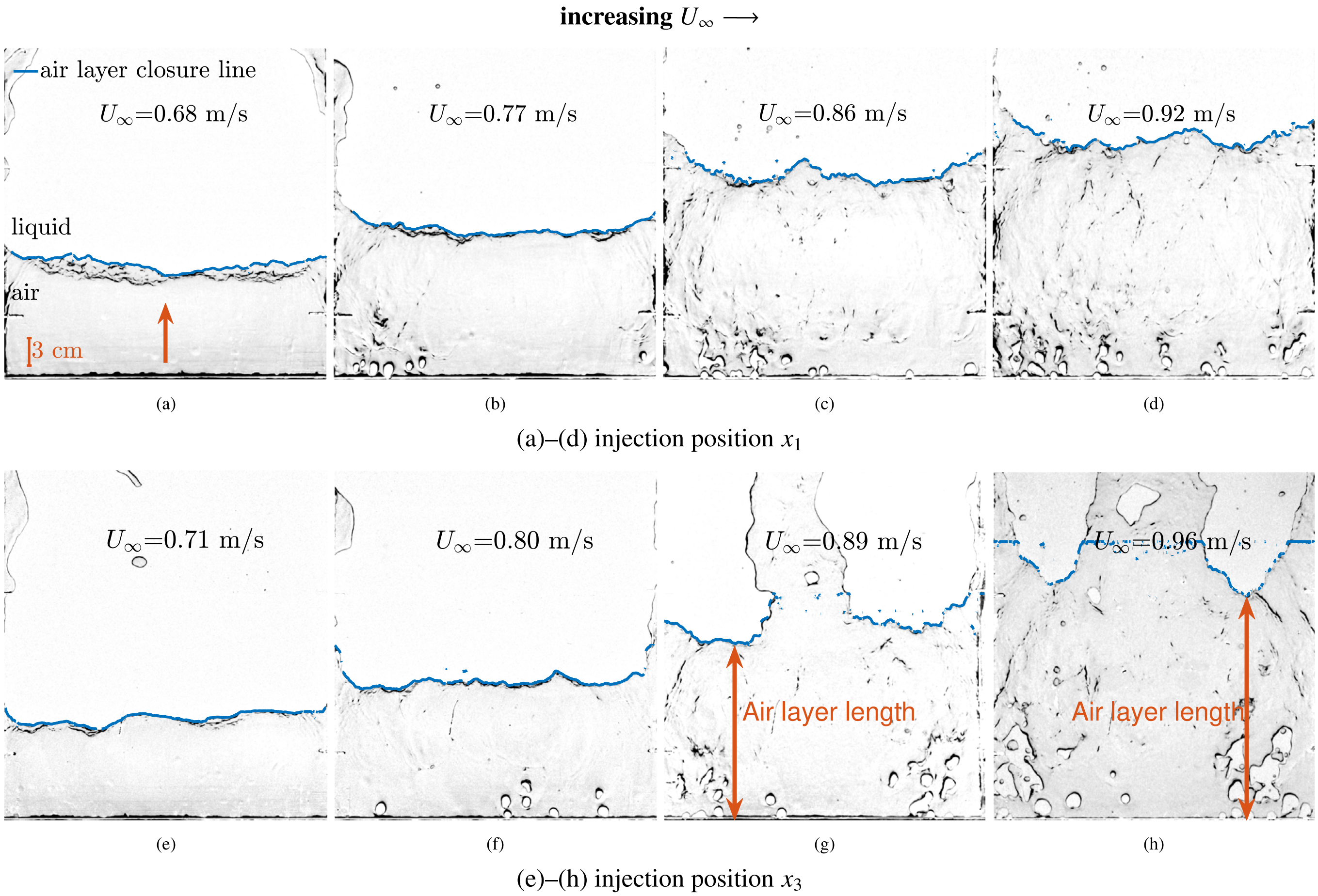

Fig. 12. Characteristic air layer images for different air injection positions and freestream velocities. For the shorter development length of $x_1 = 1.45$ m (a)–(d) and the larger development length of $x_3 = 3.95$ m (e)–(h). Flow is from down up.

exhibits a two branch behavior: the air layer closure line between the two branches is relatively smooth (especially for lower U_∞) and as such its average streamwise distance from the injector location is similar to the minimum (L_{air}). On the other hand, in the case of a thicker incoming TBL (Figs. 12(e)–12(h)) the air layer exhibits a three branch behavior: L_{air} then coincides with one of the bifurcation points of the closure line between the three branches. In this way, only the spanwise uniform region of the air layer is taken into account, while the shedding region (Fig. 8) is excluded.

The calculated L_{air} is seen to increase monotonically with U_∞ (Fig. 13), a change qualitatively observed already from the imaging data (Fig. 12). This is in line with previous studies of air cavities formed behind a BFS or cavitator (Qin et al., 2019; Zverkhovskyi, 2014) for a variety of Reynolds numbers; it has, however, not been investigated before in configurations without BFS.

As can also be seen in Fig. 13, for a specific air injection position and U_∞, L_{air} is unaffected by Q_{air} variations. This indicates that, once a certain air layer length is reached, further increasing the Q_{air} results in the air layer shedding more air through the elongated branches while the spanwise uniform region remains unchanged. Similar observations were also noted in Qin et al. (2019), where they showed an abrupt jump in the cavity length once it transitioned to the two-branch regime, but once it is reached further increasing the air flow rate had no effect. It must be noted that this is not the case for Barbaca et al. (2018), where an increase in the pressure inside the cavity (controlled by the air flow rate) resulted in an increase of L_{air} and an equilibrium air layer length existence is not reported. This could either mean that such a regime is not present in the experiments or that this regime is not yet reached.

Apart from U_∞ effects on L_{air}, morphological differences due to different incoming TBL δ are also present. For both model injectors a longer air layer is observed in the case of a lower incoming TBL δ (open markers in Fig. 13) for a specific U_∞. This is in line with the observations of Barbaca et al. (2018) for an air layer formed behind a BFS, where the pressure inside the cavity was measured. For the same pressure in the cavity (controlled by air flow rate), a lower h/δ with h being the BFS height, resulted in a smaller cavity length. The authors attributed this to a less pronounced blockage effect. Such effects are not expected in our case however. We propose that the L_{air} variation with δ is attributed to the local streamwise velocity U_{local}, defined as the mean streamwise velocity of the incoming TBL (with air, see also Section 3.2) at $y = t_{air}$. With that in mind, a thinner incoming TBL leads to a larger local velocity and a larger L_{air}. In Fig. 14, U_{local} is compared with L_{air} for the results that share the same injector model. The local streamwise velocity is computed from averaging 10 neighboring vectors at $y = t_{air}$, immediately upstream of the air layer. It can be seen that a better scaling of the L_{air} is achieved when using U_{local} as the relevant velocity scale rather than U_∞ (inserts in Fig. 14). Despite our efforts however, it appears that we cannot collapse all the data into a single figure. Further experiments with a wider parameter space are necessary to achieve this.

Finally, the measured L_{air} is compared with *half* gravity wavelength derived from the dispersion relation. In our experiments we are in the deep water regime ($d/L > 0.5$, where d is the water tunnel depth), so that the deep water approximation is considered:

$$V^2 = \frac{gL}{2\pi} \tag{3}$$

where V is the phase velocity and L is the gravity wavelength. More specifically, Butuzov (1966, 1967) using potential flow theory, derived the theoretical limiting air cavity length for which a stable cavity

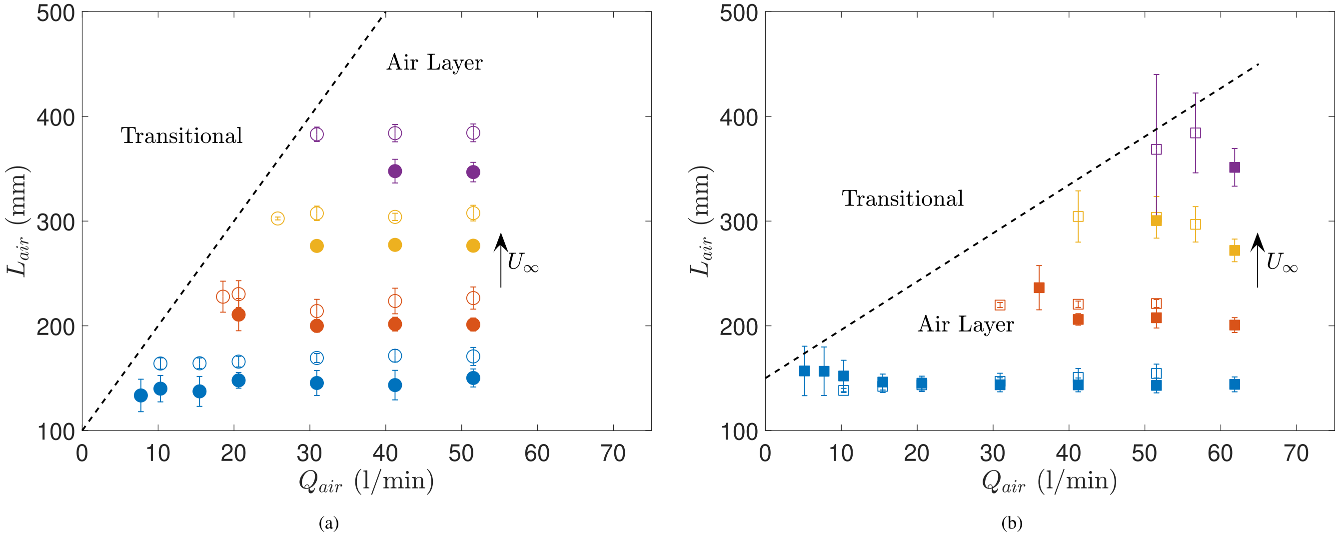

Fig. 13. Measured air layer length for different air flow rates for air injection positions (a) x_1 (open circles) and x_3 (filled circles) and (b) x_2 (open squares) and x_4 (filled squares). The vertical errorbars show the standard deviation. Dashed line indicates the boundary between transitional and air layer regimes (lower Q_{air} than then ones considered here correspond to the transitional regime). The colors indicate the different freestream velocities: $U_\infty = 0.68 - 0.72$ (blue), $U_\infty = 0.77 - 0.81$ (red), $U_\infty = 0.86 - 0.90$ (yellow), $U_\infty = 0.92 - 0.97$ (purple). See Table 2 for specific U_∞ for the different positions. (For interpretation of the references to color in this figure legend, the reader is referred to the web version of this article.)

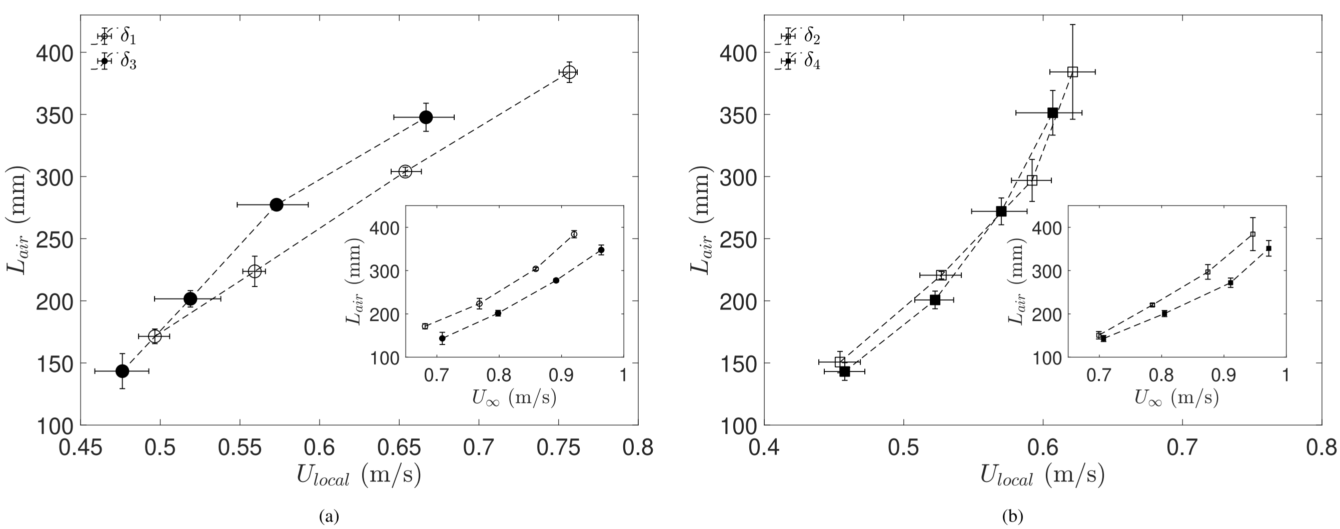

Fig. 14. Scaling of air layer length with local streamwise velocities for air injection positions (a) x_1 and x_3 (model A injector) and (b) x_2 and x_4 (model B injector). Insert: Scaling of air layer length with freestream velocities.

smoothly reattaches to a solid surface. Despite the simplicity of this model, comparison with experimental data confirmed the correlation of the air cavity length with the velocity squared (Matveev et al., 2009; Matveev, 2012, 2020). Following this work, in Fig. 15 the measured L_{air} for a specific U_∞ and various incoming δ is plotted against the *half* gravity wavelength (dashed line) and some experimental data of other studies (Qin et al., 2019; Zverkhovskyi, 2014). It can be seen that the measured L_{air} agrees reasonably well with the predicted wavelength. As mentioned before, the limiting air cavity length is derived for an air cavity forming behind a wedge or a cavitator. Despite the fact that no such inserts where used in the current experiments, a good comparison is observed especially for the lower U_∞ where the air layer resembles an air cavity shape with a higher U_{air}/U_∞ ratio (≈ 0.42) where U_{air} is defined based on Q_{air} and the injection slot area.

3.5. Effect of incoming flow conditions on regime transitions

As presented in Section 3.3, the morphological characterization of BR, TALR and ALR, revealed distinct features between the three regimes. The regime maps for each development length (incoming TBL thickness) prior to the air injection are presented in Fig. 16. While other researchers classified regimes based on drag reduction (Elbing et al., 2008) here the different regimes are determined based on the distribution of A_{nw} as the air flow rate increases (Figs. 6,7). In this section, the effect of both the freestream velocity and the incoming TBL thickness on regime transitions is discussed. The latter has not been looked at yet for a configuration without a BFS or cavitator upstream of the air injection.

In general, irrespective of incoming TBL thickness, increasing U_∞ results in an increase of the transitional and the critical air flow

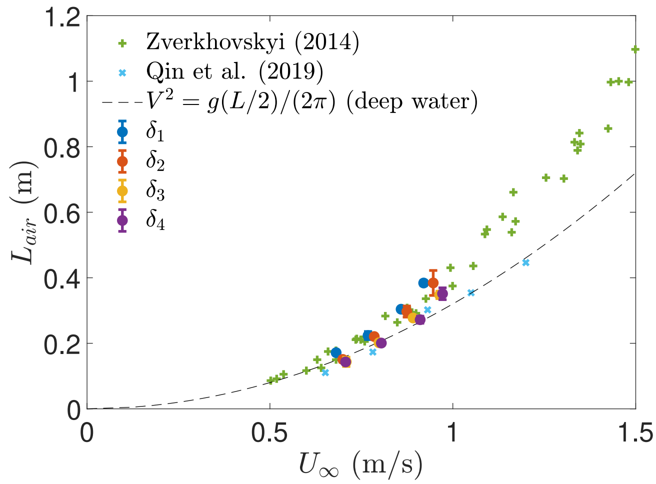

Fig. 15. Dispersion relation (water depth d = 0.58 m) for deep water (dashed line) using half gravity wavelength L/2 according to Butuzov (1966, 1967).

rates Q_{trans} and Q_{crit}: for a higher liquid U_∞ more air is needed to transition from one regime to another. This is in agreement with the results of Elbing et al. (2008), which were obtained in a much higher Reynolds number flow. In the study of Barbaca et al. (2018), the regime transitions were not studied specifically, but it was noted that for higher Froude numbers, more air is needed to achieve a certain cavity pressure. In addition, for the incoming TBL thicknesses considered here, there is an evident divergence between the two lines demarcating the regime regions for increasing U_∞.

To facilitate comparison of the critical threshold indicating the onset of ALR with other studies, the critical nominal air flow rate $t_{\alpha,crit}$ (Eq. (1)) is used. While both Elbing et al. (2008) (Re_x $\mathcal{O}(10^8)$) and Peifer et al. (2020) (Re_x $\mathcal{O}(10^6)$) found that a $t_{\alpha,crit} > 6$ mm is needed to a establish an air layer below a hydraulically smooth plate, in the current experiments much lower values are found (0.2 – 0.4 mm for the lower velocities measured and 0.9 – 1.7 mm for the highest). Although extrapolation to lower velocities from the much higher Reynolds data range of Elbing et al. (2008) is difficult, it is found that $t_{\alpha,crit}$ over predicts the critical air flow in the case of the lower velocities while it is under-predicted for higher velocities. It must be noted that Jang et al. (2014) also observed a discrepancy on the $t_{\alpha,crit}$ prediction. This suggests that more parameters other than freestream velocity, critical air flow rate and span of the test section affect the onset of the air layer regime.

Different regime maps are presented for the different incoming TBL thicknesses; results are presented for the model A injector (incoming TBL δ_1 and δ_3), but similar results were acquired for model B. The effect of TBL conditions is reflected in two main differences in the regime plots. To begin with, a lower air flow rate was needed to transition from the BR to the TALR regime in the case of the thicker incoming TBL ($\delta_3 > \delta_1$). As explained in the previous section, based on the calculated t_{air} a lower local velocity is present at the air–water interface in the case of injection position x_3. That could act to enable rather than inhibit the transition from the BR to the TALR regime. To summarize:

$$\begin{aligned} &\delta_3 > \delta_1 \\ &U_{local,3} < U_{local,1} \\ &Q_{trans,3} < Q_{trans,1} \end{aligned} \tag{4}$$

It must be noted that this was not the case for lower velocity (U_∞ = 0.68 m/s) but that could be also attributed to the resolution of the rotameter (2 l/min).

That being said, a higher air flow rate was needed to transition from the TALR to ALR, in the case of a thicker incoming TBL:

$$Q_{crit,3} > Q_{crit,1} \tag{5}$$

Again the lower velocity is excluded from this trend. By definition, the ALR regime is characterized by a region of spanwise uniformity (Fig. 8). Since the air layer interface lies in the wake region ($t_{air}/\delta_3 \approx 0.1-0.17$) in the case of incoming TBL δ_3, larger spanwise fluctuations of the streamwise velocity are expected than in the case of incoming TBL δ_1 ($t_{air}/\delta_1 \approx 0.26-0.5$). Since no quantitative data on the streamwise–spanwise incoming TBL were acquired in the experiments, a direct correlation of the air phase and the incoming spanwise TBL structures cannot be established, but it is hypothesized that larger spanwise fluctuations could delay the creation the onset of the ALR. This opposite trend of Q_{trans} and Q_{crit} becomes evident as the TALR gets wider with increasing TBL thickness.

4. Summary & conclusions

The purpose of the current study is to investigate the effect of incoming flow conditions on the different regimes in air lubrication. The different air phase regimes are created along a flat plate spatially developing TBL without the use of a BFS upstream of the air injection position. Various incoming flow conditions are achieved by changing the incoming liquid freestream velocity and the incoming liquid TBL thickness.

For different liquid freestream velocities ($U_\infty = 0.65-1$ m/s) and air flow rates ($Q_{air} = 5-52$ l/min) and irrespectively of the incoming TBL thickness, three air phase regimes are observed: the bubbly regime (BR), the transitional air layer regime (TALR), and the air layer regime (ALR). The percentage of non-wetted area is found to increase with increasing Q_{air} for the BR and ultimately peak at the TALR before relaxing to a constant non-wetted area percentage at the ALR. Once the latter is reached, a three or two branch air cavity is observed, the length of which is predicted reasonably well by a half gravity wave for a specific U_∞ and water depth. Having said that, increasing U_∞ results in an increase of the air layer length. In addition, a systematically longer air cavity is observed for a thinner incoming TBL, a phenomenon that the dispersion relation cannot explain, but can be attributed to an increase in velocity, when local (wall-normal varying) instead of freestream velocities are considered. This is a corollary of higher t_{air}/δ ratios for thinner incoming TBLs and also explains why the dispersion relation based on U_∞ cannot predict the trend.

The transitional and critical air flow rates (Q_{trans} and Q_{crit}, respectively) are also measured. In line with previous studies it is concluded that for increasing U_∞ both Q_{trans} and Q_{crit} are increasing. In addition, it is shown that the incoming TBL thickness has an effect on the transition points. More specifically, it is shown that for the same U_∞, an increasing incoming TBL thickness results in a decrease of Q_{trans} and an increase of the Q_{crit}. It is hypothesized that the former can be explained when the local (wall-varying) velocity at the air–water interface is considered, while the later is attributed to the change in t_{air}/δ (0.17 to 0.3), both measured with PIV, and the associated different incoming TBL structures.

In conclusion, we have shown that the incoming TBL conditions have an effect on both the regime transition points and the characteristics of the air layer (once it is formed). Furthermore, our results indicate that using the local velocity U_{local} at the air–water interface and the ratio of the air layer to incoming TBL thickness t_{air}/δ improves scaling and provides an additional physical interpretation in a way that global flow parameters (e.g. U_∞) cannot explain. In the future, expanding the data range and incorporating more parameters is needed to further improve and validate the scaling. This work will help in designing efficient drag reduction mechanisms for ships.

CRediT authorship contribution statement

Lina Nikolaidou: Writing – original draft, Visualization, Validation, Methodology, Investigation, Formal analysis, Data curation, Conceptualization. **Angeliki Laskari:** Writing – review & editing, Supervision,

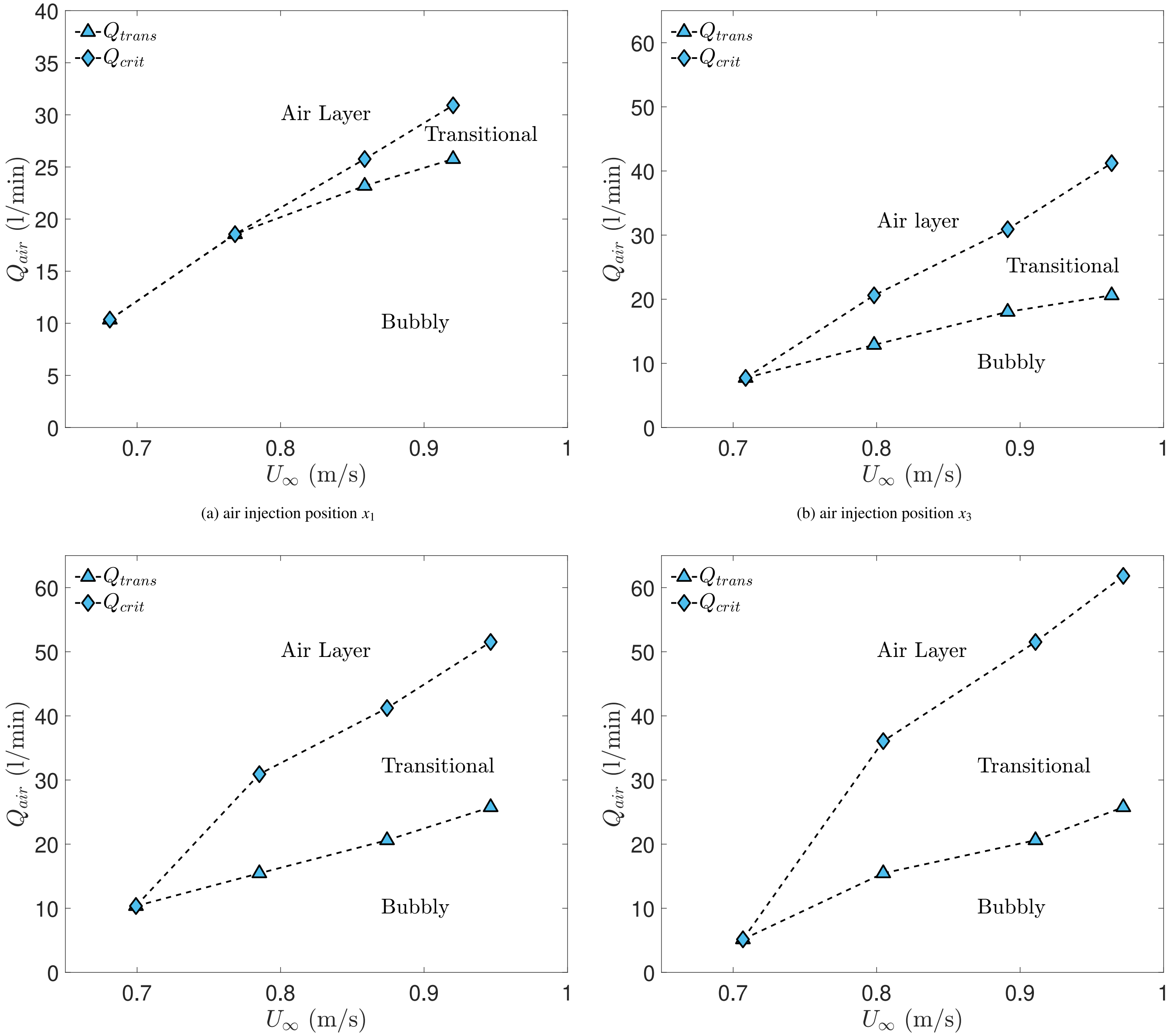

(a) air injection position x_1

(b) air injection position x_3

(c) air injection position x_2

(d) air injection position x_4

Fig. 16. Regime maps for four different air injection positions (incoming TBL thicknesses). The regions of the different regimes are marked for clarity and the dashed lines demarcate the regimes.

Methodology, Conceptualization. **Tom van Terwisga:** Writing – review & editing, Supervision, Methodology, Funding acquisition, Conceptualization. **Christian Poelma:** Writing – review & editing, Supervision, Methodology, Funding acquisition, Conceptualization.

Declaration of competing interest

The authors declare that they have no known competing financial interests or personal relationships that could have appeared to influence the work reported in this paper.

Data availability

Data will be made available on request.

Acknowledgments

This work is part of the public–private research program "Water Quality in Maritime Hydrodynamics" (AQUA) project P17-07. The support by the Netherlands Organisation for Scientific Research (NWO) Domain Applied and Engineering Sciences, and project partners is gratefully acknowledged.

Appendix A. Supplementary data

Supplementary material related to this article can be found online at https://doi.org/10.1016/j.ijmultiphaseflow.2024.104948.

References

Anand, A., 2021. Experimental Investigation of Influence of an Air Cavity on a Turbulent Boundary Layer Using PIV. TU Delft, the Netherlands, http://resolver.tudelft.nl/uuid:a80a278f-6ca8-4356-a5b0-461b9f679d68.

Barbaca, L., Pearce, B.W., Brandner, P.A., 2017. Experimental study of ventilated cavity flow over a 3-D wall-mounted fence. Int. J. Multiph. Flow 97, 10–22.

Barbaca, L., Pearce, B.W., Brandner, P.A., 2018. An experimental study of cavity flow over a 2-D wall-mounted fence in a variable boundary layer. Int. J. Multiph. Flow 105, 234–249.

Bidkar, R.A., Leblanc, L., Kulkarni, A.J., Bahadur, V., Ceccio, S.L., Perlin, M., 2014. Skin-friction drag reduction in the turbulent regime using random-textured hydrophobic surfaces. Phys. Fluids 26 (8).
Brennen, C.E., 2014. Cavitation and Bubble Dynamics. Cambridge University Press.
Butuzov, A., 1966. Limiting parameters of an artificial cavity formed on the lower surface of a horizontal wall. Fluid Dyn. 1 (2), 116–118.
Butuzov, A., 1967. Artificial cavitation flow behind a slender wedge on the lower surface of a horizontal wall. Fluid Dyn. 2 (2), 56–58.
Ceccio, S.L., 2010. Friction drag reduction of external flows with bubble and gas injection. Annu. Rev. Fluid Mech. 42, 183–203.
Charruault, F., Greidanus, A., Breugem, W.P., Westerweel, J., 2018. A dot tracking algorithm to measure free surface deformations. In: Proceedings 18th International Symposium on Flow Visualization. ETH Zurich.
Clauser, F.H., 1956. The turbulent boundary layer. Adv. Appl. Mech. 4, 1–51.
De Graaff, D.B., Eaton, J.K., 2000. Reynolds-number scaling of the flat-plate turbulent boundary layer. J. Fluid Mech. 422, 319–346.
de Silva, C.M., Kevin, K., Baidya, R., Hutchins, N., Marusic, I., 2018. Large coherence of spanwise velocity in turbulent boundary layers. J. Fluid Mech. 847, 161–185.
Dean, B., Bhushan, B., 2010. Shark-skin surfaces for fluid-drag reduction in turbulent flow: a review. Phil. Trans. R. Soc. A 368 (1929), 4775–4806.
Dennis, D.J., Nickels, T.B., 2011. Experimental measurement of large-scale three-dimensional structures in a turbulent boundary layer. Part 2. Long structures. J. Fluid Mech. 673, 218–244.
Du, P., Wen, J., Zhang, Z., Song, D., Ouahsine, A., Hu, H., 2017. Maintenance of air layer and drag reduction on superhydrophobic surface. Ocean Eng. 130, 328–335.
Elbing, B.R., Mäkiharju, S., Wiggins, A., Perlin, M., Dowling, D.R., Ceccio, S.L., 2013a. On the scaling of air layer drag reduction. J. Fluid Mech. 717, 484–513.
Elbing, B.R., Perlin, M., Dowling, D.R., Ceccio, S.L., 2013b. Modification of the mean near-wall velocity profile of a high-Reynolds number turbulent boundary layer with the injection of drag-reducing polymer solutions. Phys. Fluids 25 (8).
Elbing, B.R., Winkel, E.S., Lay, K.A., Ceccio, S.L., Dowling, D.R., Perlin, M., 2008. Bubble-induced skin-friction drag reduction and the abrupt transition to air-layer drag reduction. J. Fluid Mech. 612, 201–236.
Fitzpatrick, P., Jang, J., Kim, B., Kim, J., Lee, J., McStay, P., Raptakis, G., et al., 2017. Full scale applications of air lubrication for reduction of ship frictional resistance. In: SNAME Maritime Convention. The Society of Naval Architects and Marine Engineers.
Fukuda, K., Tokunaga, J., Nobunaga, T., Nakatani, T., Iwasaki, T., Kunitake, Y., 2000. Frictional drag reduction with air lubricant over a super-water-repellent surface. J. Mar. Sci. Technol. 5, 123–130.
García-Mayoral, R., Jiménez, J., 2011. Drag reduction by riblets. Philos. Trans. R. Soc. Lond. Ser. A Math. Phys. Eng. Sci. 369 (1940), 1412–1427.
Gose, J.W., Golovin, K., Boban, M., Mabry, J.M., Tuteja, A., Perlin, M., Ceccio, S.L., 2018. Characterization of superhydrophobic surfaces for drag reduction in turbulent flow. J. Fluid Mech. 845, 560–580.
Hao, W., Yongpeng, O., Qing, Y., 2019. Experimental study of air layer drag reduction on a flat plate and bottom hull of a ship with cavity. Ocean Eng. 183, 236–248.
Harleman, M., Delfos, R., Van Terwisga, T., Westerweel, J., 2011. Dispersion of bubbles in fully developed channel flow. J. Phys. Conf. Ser. 318 (5), 052007.
Hoang, C., Toda, Y., Sanada, Y., et al., 2009. Full scale experiment for frictional resistance reduction using air lubrication method. In: The Nineteenth International Offshore and Polar Engineering Conference. International Society of Offshore and Polar Engineers.
IMO, 2023. IMO strategy on reduction of GHG emissions from ships. MEPC 377, 80.
Jang, J., Choi, S.H., Ahn, S.M., Kim, B., Seo, J.S., 2014. Experimental investigation of frictional resistance reduction with air layer on the hull bottom of a ship. Int. J. Nav. Archit. Ocean Eng. 6 (2), 363–379.
Jooss, Y., Li, L., Bracchi, T., Hearst, R.J., 2021. Spatial development of a turbulent boundary layer subjected to freestream turbulence. J. Fluid Mech. 911.
Kevin, K., Monty, J., Hutchins, N., 2019. The meandering behaviour of large-scale structures in turbulent boundary layers. J. Fluid Mech. 865, R1.
Kim, D., Moin, P., 2010. Direct numerical study of air layer drag reduction phenomenon over a backward-facing step. In: Annual Research Briefs. Center for Turbulence Research, pp. 351–363, https://scholar.google.com/scholar?hl=en&as_sdt=0%2C5&q=Direct+numerical+study+of+air+layer+drag+reduction+phenomenon+over+a+backward-facing+step.&btnG=.
Kim, S., Oshima, N., Park, H.J., Murai, Y., 2021. Direct numerical simulation of frictional drag modulation in horizontal channel flow subjected to single large-sized bubble injection. Int. J. Multiph. Flow 145, 103838.
Kim, Y.-R., Steen, S., 2023. Potential energy savings of air lubrication technology on merchant ships. Int. J. Nav. Archit. Ocean Eng. 100530.
Larsson, L., 2010. Ship resistance and flow. Published by the Society of Naval Architects and Marine Engineers, SNAME, the Principles of Naval Architecture Series, ISBN: 978-0-939773-76-3.
Lay, K.A., Yakushiji, R., Mäkiharju, S., Perlin, M., Ceccio, S.L., 2010. Partial cavity drag reduction at high Reynolds numbers. J. Ship Res. 54 (2), 109–119.
Lu, J., Fernández, A., Tryggvason, G., 2005. The effect of bubbles on the wall drag in a turbulent channel flow. Phys. Fluids 17 (9), 095102.
Madavan, N., Deutsch, S., Merkle, C., 1984. Reduction of turbulent skin friction by microbubbles. Phys. Fluids 27 (2), 356–363.
Madavan, N., Deutsch, S., Merkle, C., 1985. Measurements of local skin friction in a microbubble-modified turbulent boundary layer. J. Fluid Mech. 156, 237–256.
Mäkiharju, S.A., Perlin, M., Ceccio, S.L., 2012. On the energy economics of air lubrication drag reduction. Int. J. Nav. Archit. Ocean Eng. 4 (4), 412–422.
Matveev, K.I., 2012. Two-dimensional modeling of stepped planing hulls with open and pressurized air cavities. Int. J. Nav. Archit. Ocean Eng. 4 (2), 162–171.
Matveev, K.I., 2020. Simplified model for unsteady air cavities under ship hulls. Proc. Inst. Mech. Eng. M 234 (1), 100–107.
Matveev, K.I., Burnett, T.J., Ockfen, A.E., 2009. Study of air-ventilated cavity under model hull on water surface. Ocean Eng. 36 (12–13), 930–940.
McCormick, M.E., Bhattacharyya, R., 1973. Drag reduction of a submersible hull by electrolysis. Nav. Eng. J. 85 (2), 11–16.
Mizokami, S., Kawakita, C., Kodan, Y., Takano, S., Higasa, S., Shigenaga, R., 2010. Experimental study of air lubrication method and verification of effects on actual hull by means of sea trial. Mitsubishi Heavy Ind. Technol. Rev. 47 (3), 41–47.
Murai, Y., 2014. Frictional drag reduction by bubble injection. Exp. Fluids 55 (7), 1773.
Nikolaidou, L., Laskari, A., van Terwisga, T., Poelma, C., 2021. On the characteristics of air layer regimes. In: 11th International Symposium on Cavitation 202. CAV2021, The Society of Naval Architects of Korea, pp. 386–391, https://scholar.google.com/scholar?hl=en&as_sdt=0%2C5&q=+On+the+characteristics+of+air+layer+regimes&btnG=&oq=ON+T.
Otsu, N., 1979. A threshold selection method from gray-level histograms. IEEE Trans. Syst. Man Cybern. 9 (1), 62–66.
Pearce, B., Brandner, P., Foster, S., 2015. Ventilated cavity flow over a backward-facing step. J. Phys. Conf. Ser. 656 (1), 012164.
Peifer, B.C., Callahan-Dudley, C., Mäkiharju, S.A., 2020. Air layer on superhydrophobic surface for frictional drag reduction. J. Ship Res. 64 (2).
Perlin, M., Dowling, D.R., Ceccio, S.L., 2016. Freeman scholar review: passive and active skin-friction drag reduction in turbulent boundary layers. J. Fluids Eng. 138 (9).
Qin, S., Wu, Y., Wu, D., Hong, J., 2019. Experimental investigation of ventilated partial cavitation. Int. J. Multiph. Flow 113, 153–164.
Sanders, W.C., Winkel, E.S., Dowling, D.R., Perlin, M., Ceccio, S.L., 2006. Bubble friction drag reduction in a high-Reynolds-number flat-plate turbulent boundary layer. J. Fluid Mech. 552, 353, https://www.cambridge.org/core/journals/journal-of-fluid-mechanics/article/bubble-friction-drag-reduction-in-a-highreynoldsnumber-flatplate-turbulent-boundary-layer/AE49975D9D126AD2E06F699901D2FBDF.
Silberschmidt, N., Tasker, D., Pappas, T., Johannesson, J., 2016. Silverstream system-air lubrication performance verification and design development. In: Conference of Shipping in Changing Climate, Newcastle, UK. pp. 10–11, https://scholar.google.com/scholar?hl=en&as_sdt=0%2C5&q=Silberschmidt%2C+N.%2C+Tasker%2C+D.%2C+Pappas%2C+T.%2C+Johannesson%2C+J.%2C+2016.+Silverstream+systemair+lubrication+performance+verification+and+design+development.+In%3A+Conference+of+Shipping+in+Changing+Climate.+Newcastle%2C+UK%2C+pp.+10%E2%80%9311.&btnG=.
Verschoof, R.A., Van Der Veen, R.C., Sun, C., Lohse, D., 2016. Bubble drag reduction requires large bubbles. Phys. Rev. Lett. 117 (10), 104502.
Wang, D., Sun, Q., Hokkanen, M.J., Zhang, C., Lin, F.Y., Liu, Q., Zhu, S.P., Zhou, T., Chang, Q., He, B., et al., 2020. Design of robust superhydrophobic surfaces. Nature 582 (7810), 55–59.
Westerweel, J., Scarano, F., 2005. Universal outlier detection for PIV data. Exp. Fluids 39, 1096–1100.
Winkel, E., Oweis, G., Vanapalli, S., Dowling, D., Perlin, M., Solomon, M., Ceccio, S., 2009. High-Reynolds-number turbulent boundary layer friction drag reduction from wall-injected polymer solutions. J. Fluid Mech. 621, 259–288.
Woud, J.K., Stapersma, D., 2002. Design of Propulsion and Electric Power Generation Systems. IMarEST.
Xu, M., Grabowski, A., Yu, N., Kerezyte, G., Lee, J.W., Pfeifer, B.R., et al., 2020. Superhydrophobic drag reduction for turbulent flows in open water. Phys. Rev. Appl. 13 (3), 034056.
Yoon, K., Qin, S., Shao, S., Hong, J., 2020. Internal flows of ventilated partial cavitation. Exp. Fluids 61 (4), 1–15.
Zverkhovskyi, O., 2014. Ship Drag Reduction by Air Cavities (Ph.D. thesis). TU Delft, http://dx.doi.org/10.4233/uuid:a5754f75-55c1-4407-bebb-41458e6c9a11.